Research Square

Preprints are preliminary reports that have not undergone peer review.
They should not be considered conclusive, used to inform clinical practice,
or referenced by the media as validated information.

Analysis and Experimental Study of Obstacle-Crossing Performance of Natural Gas Pipeline Inspection Robots

Shengqian Ruan
Yangtze University
Lei Shi
shilei0909@163.com

Yangtze University
Penggao Guo
China University of Petroleum, Beijing
Wangliang Xiang
Yangtze University
Xiangjin Lin
Yangtze University

Article

Keywords: natural gas pipeline, internal inspection robot, obstacle-crossing performance, dynamic simulation, scaled-down experiments

Posted Date: July 16th, 2026

DOI: https://doi.org/10.21203/rs.3.rs-10289826/v1

License: This work is licensed under a Creative Commons Attribution 4.0 International License.
Read Full License

Additional Declarations: No competing interests reported.

Analysis and Experimental Study of Obstacle-Crossing Performance of Natural Gas Pipeline Inspection Robots

Shengqian Ruan[1], Lei Shi[1]✉, Penggao Guo[2], Wangliang Xiang[1], Xiangjin Lin[1]

1.School of Mechanical Engineering,Yangtze University,Jingzhou,434023,China.

2.School of Petroleum Engineering,China University of Petroleum-Beijing,18 Fuxue Road, Changping, Beijing, P.R.China 102249

Corresponding author: Lei Shi; ✉email: shilei0909@163.com.

Abstract

Defects in the circumferential welds of long-distance natural gas pipelines are a major threat to pipeline operational safety. This paper presents the design of an in-pipe inspection robot platform for DN1016 large-diameter natural gas pipelines, featuring three short sections connected in series and an umbrella-shaped link mechanism for adaptive diameter adjustment. A quasi-static theoretical model for the drive wheel crossing the circumferential weld was established, and analytical expressions for the maximum obstacle-crossing height were derived based on both traction boundary conditions and anti-slip adhesion conditions. An obstacle-crossing simulation model was developed using ADAMS multibody dynamics software, and parametric transient dynamic analyses were conducted within a speed range of 0.12 – 1.2 m/s. A 1:5 scale-down proof-of-concept prototype was developed, and an acrylic simulated pipeline test rig was constructed to conduct experiments on bend passability and circumferential weld obstacle crossing. The research results indicate that the design dimensions of the robot—a single-section body of 1,450 mm and a universal joint of 183 mm—meet the geometric passability requirements for a 5D bend (R = 5,080 mm); the maximum obstacle-crossing height is approximately 8.5 mm, meeting the engineering standard of a circumferential weld reinforcement height of ⩽6 mm within the pipe; at the recommended obstacle-crossing speed of 0.24 m/s, the peak torque of the drive wheel is 12.4 N • m, with a vertical displacement of the center of mass of only 0.25 mm and a displacement attenuation rate exceeding 95%; the scaled-down experiments validated the radial yielding capacity of the variable-diameter mechanism and the feasibility of obstacle crossing.

Keywords: natural gas pipeline; internal inspection robot; obstacle-crossing performance; dynamic simulation; scaled-down experiments

1 Introduction

As of the end of 2020, the total length of China's long-distance natural gas pipelines had reached nearly 110,000 kilometers[1–3]. Behind the massive volume of gas transported by these pipelines lie unavoidable operational risks—methane, the medium transported through the pipelines, is inherently flammable and explosive, and any leak can quickly escalate into a large-scale fire or even an explosion. Statistics on multiple cracking incidents involving newly constructed pipelines in China since 2011 indicate that the causes of these accidents largely stem from the combined effects of welding defects and external loads, with cracks predominantly occurring on the inner walls of the pipelines. A comprehensive analysis of accident investigation results reveals that defects in circumferential welds and localized deformation of the pipe body are the primary causes of safety incidents in long-distance pipelines, making periodic internal inspections of in-service pipelines indispensable.

Pipeline inspection robots equipped with non-destructive testing devices for long-distance automated inspections represent the mainstream technological solution in this field[4–7]. However, the physical passability of the inspection platform is a key factor limiting practical application—local obstacles caused by variations in pipe diameter, bends, weld bead height, and misalignment between the weld and the pipe wall all hinder the robot's movement. To address passability issues in complex pipeline geometries, scholars both domestically and internationally have proposed various configurable robot solutions, with multi-segment series configurations and adaptive diameter changes being the mainstream technical approaches. When faced with complex pipeline geometries, most existing internal inspection systems lack flexible, adaptive diameter-adjustment capabilities; instances of drive wheel slippage, body instability, and even jamming are not

uncommon. Jamming failures are also a key focus of optimization for foreign inspection equipment; relevant research has reduced resistance fluctuations during obstacle crossing by optimizing support mechanisms. Therefore, designing a load-bearing chassis for inspection platforms that features adaptive diameter adjustment and obstacle-crossing capabilities holds significant engineering importance[8–11].

To address the above issues, this paper designs a pipeline inspection robot platform featuring three short sections connected in series and an umbrella-shaped link for adaptive diameter adjustment, using the DN1016 large-diameter natural gas pipeline as the application context. A systematic study of the robot's obstacle-crossing performance is conducted from three aspects: theoretical modeling, dynamic simulation, and scaled-down experiments.

2 Overall Structure of the Robot

2.1 Operating Conditions Analysis and Design Parameters

The pipeline inspection robot designed in this paper is suitable for DN1016 long-distance natural gas trunk lines. The core design constraints are centered on obstacle-crossing capability: first, it accommodates an inner diameter variation range of 910–1030 mm to ensure passage through 5D bends; the traction system incorporates torque redundancy to ensure stable operation on a 10° incline and the ability to traverse 3–5 mm misaligned circumferential welds, thereby defining the operational boundaries for obstacle-crossing performance research[12]. Second, the chassis suspension must possess radial centering and shock-absorbing capabilities to damp transient vibrations generated during obstacle crossing, providing a basis for evaluating smoothness during obstacle navigation. Third, with the entire machine fully loaded at approximately 300 kg and operating at speeds ranging from 0 to 1 m/s, key load-bearing components must meet strength and stiffness requirements under dynamic loads during obstacle crossing, forming the load basis for obstacle-crossing dynamic analysis. This paper establishes the overall performance parameters and key technical indicators for the robotic platform; these indicators will serve as design inputs for subsequent structural design, theoretical modeling, and component selection. Specific system parameters are shown in Table 1.

Table 1 Design index of inspection robot for natural gas pipeline

Index Type	Parameter Item	Design Target Value	Remarks
Geometric Parameters	Applicable Pipe Diameter	DN1016	
	Diameter Adaptation Range	910-1030mm	Adapt to 12% diameter variation and ovality
	Bend Passing Capacity	5D	Curvature radius R=5080mm
	Obstacle-Crossing Height	6mm	Adapt to weld reinforcement and misalignment
Environmental Parameters	Operating Temperature Range	-20~60℃	Adapt to wide-temperature operating environment
	Ambient Pressure	5-10Mpa	Adapt to working conditions of high-pressure transmission pipelines
Motion Performance	Operating Speed Range	0-1m/s	Capable of variable-speed operation
	Cruising Mileage	> 150km	Meet the distance requirement between adjacent stations
	Maximum Climbing Angle	10°	Adapt to undulating pipe sections in mountainous areas
Overall Machine Parameters	Total Mass	≤300kg	Satisfy payload carrying requirements

2.2 Overall Robot Configuration Scheme

The robot adopts an overall configuration consisting of three short segments connected in series: from front to back, these are the traction segment, the inspection segment, and the power generation segment, with adjacent segments connected via universal joints. The entire machine employs a distributed active-wheel drive system, with six sets of drive wheels evenly distributed around the circumference (two sets per segment), each set driven by an independent 57BLF02 brushless DC motor. The axial length of a single segment is 1,450 mm, and the length of the universal joint's central articulation is 183 mm[14, 25]. This configuration ensures sufficient traction while enabling attitude coordination between segments through the degrees of freedom provided by the universal joints[15–19].

2.3 Adaptive Diameter-Adjustment Mechanism

The adaptive diameter-adjustment mechanism is a core functional component that enables the robot to adapt to varying pipe diameters and yield to obstacles. This mechanism employs an umbrella-shaped link structure: the central slider slides axially along the main shaft and is connected to the support wheel frame via a planar link mechanism composed of three sets of main and auxiliary arms evenly distributed circumferentially, converting the slider's axial displacement into the radial extension and retraction motion of the support wheels. A preloaded spring assembly mounted on the main shaft constantly applies an axial thrust toward the pipe wall to the central slider, maintaining constant contact pressure between the support wheels and the inner pipe wall. When the pipe diameter changes or a radial obstacle is encountered, the

normal reaction force acting on the support wheels drives the central slider via the linkages, compressing or releasing the spring to enable the wheel assembly to adaptively retract and return to its original position radially. This mechanism enables passive adaptive centering in pipes with an inner diameter of approximately 978–986 mm and provides a radial clearance of about 6 mm for obstacle clearance, coordinating the radial displacement of each wheel without the need for active control. The travel drive system and the diameter-adjustment mechanism are independent of each other: the drive motor is mounted on a motor bracket; a 57BLF02 brushless DC motor is used to transmit power to the wheel assembly via a bevel gear reduction unit. The individual sections are connected via cross-shaft universal joint couplings, which provide angular compensation in two orthogonal directions, enabling the series-connected sections to deflect in a coordinated manner within curved pipes[20–23].

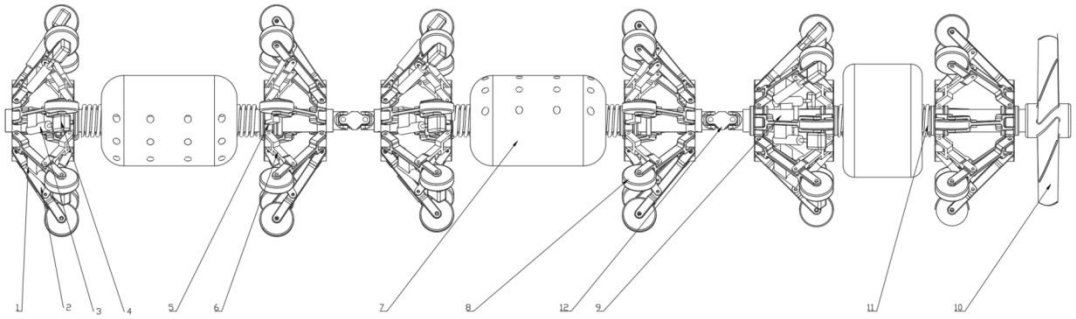
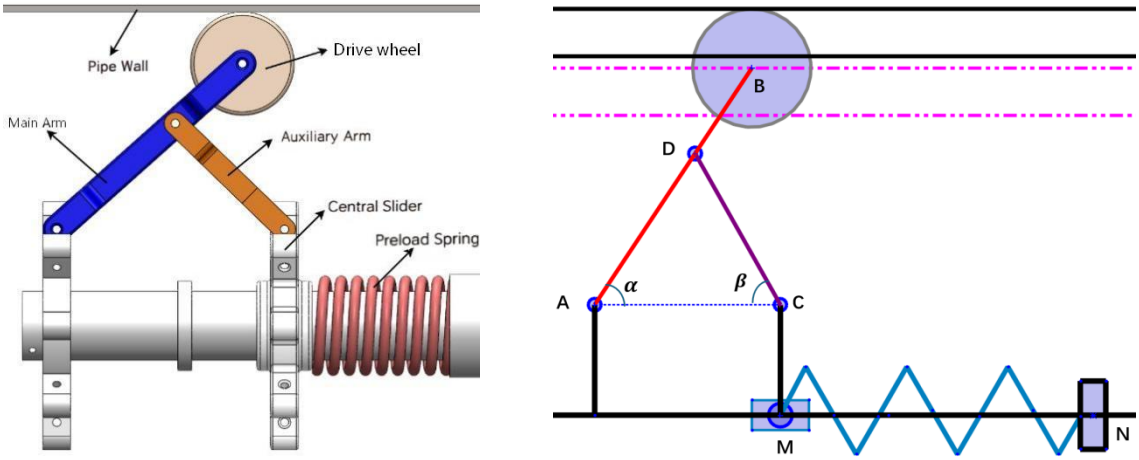


Fig. 1 Schematic Diagram of Robot Traction Section (1 – Motor Mount Support 2 – Main Arm 3 – Drive Motor 4 – Bevel Gear 5 – Central Slider 6 – Auxiliary Arm 7 – Generator Cabin 8 – Drive Wheel 9 – Main Shaft 10 – Power Generation Fan Blade 11 – Preload Spring 12 – Cross-Shaft Universal Joint Coupling)

2.4 Kinematic Analysis of the Variable-Diameter Mechanism

Based on the above assumptions, a geometric and force analysis model for the drive wheel's obstacle-crossing conditions was established.



(a) Structural Schematic of Variable-Diameter Mechanism

(b) Schematic Diagram of Geometric Parameters for Diameter Adaptation Mechanism

Fig. 2 Variable diameter mechanism structure and kinematics principle diagram

The schematic diagram of the mechanism is shown in Figure 2. A local plane Cartesian coordinate system is established with fixed hinge joint A as the coordinate origin (0,0) and the horizontal auxiliary line AC as the X-axis. The length of the main support arm AB is denoted as L1; the distance from auxiliary arm hinge joint D to point A is LAD; the length of thrust auxiliary arm DC is L2. The included angle between main arm AB and the horizontal X-axis is α, and the included angle between auxiliary arm DC and the horizontal X-axis is β. Since slider C can only slide along the horizontal guide rail, points D, B and C satisfy the following geometric constraint equation:

$$\begin{aligned} y_D &= L_{AD}\sin\alpha = L_2\sin\beta \\ x_C &= x_D + x_{DC} = L_{AD}\cos\alpha + L_2\cos\beta \\ y_B &= L_1\sin\alpha \end{aligned} \tag{1}$$

Perform a total differential on both sides of the above displacement constraint equation simultaneously to derive the transient micro-displacement mapping relationships for each hinge point.

$$\begin{aligned} L_{AD}\cos\alpha\cdot d\alpha &= L_2\cos\beta\cdot d\beta \\ d\beta &= \frac{L_{AD}\cos\alpha}{L_2\cos\beta}\cdot d\alpha \\ dx_C &= -L_{AD}\sin\alpha\cdot d\alpha - L_2\sin\beta\cdot d\beta \end{aligned} \tag{2}$$

Substitute the relational expression of dβ into the above formula and simplify using trigonometric identities:

$$\begin{aligned} dx_C &= -L_{AD}\frac{\sin(\alpha+\beta)}{\cos\beta}\cdot d\alpha \\ dy_B &= L_1\cos\alpha\cdot d\alpha \end{aligned} \tag{3}$$

Substitute dα into the equation for dx_C to eliminate the intermediate variable angular velocity, and directly obtain the instantaneous Jacobian transmission ratio J between the axial displacement of the central slider and the radial displacement of the end drive wheel:

$$J = \left|\frac{dx_C}{dy_B}\right| = \left|-L_{AD}\frac{\sin(\alpha+\beta)}{\cos\beta}\cdot\frac{1}{L_1\cos\alpha}\right| = \frac{L_{AD}}{L_1}\cdot\frac{\sin(\alpha+\beta)}{\cos\alpha\cdot\cos\beta} \tag{4}$$

The derived kinematic equations show that the transmission ratio of this mechanism exhibits nonlinear behavior, with its value changing dynamically as the opening angle of the main support arm varies.

Based on the principle of virtual work, when a system is in static equilibrium and undergoes virtual displacements, the sum of the virtual work done by all active forces equals zero. For a single suspension mechanism group, let F_S denote the axial thrust exerted on the slider by the central compression spring, and the total radial preload generated by the contact between eight support wheels and the pipe wall be $8F_p$. During virtual displacement, the spring thrust performs positive work, while the radial reaction force from the pipe wall performs negative work. Taking friction losses at hinges and sliders in the mechanism into comprehensive consideration, the overall mechanical transmission efficiency of the system is set as $\eta = 0.85$. The virtual work equilibrium equation of the system is established as follows:

$$F_s\cdot|dx_C|\cdot\eta = 8\cdot F_p\cdot|dy_B| \tag{5}$$

Substitute the kinematic transmission ratio into the above formula to derive the relational expression between the radial preload F_p of a single wheel and the central spring thrust F_S.

$$F_p = \frac{F_s\cdot\eta}{8}\cdot\frac{|dx_C|}{|dy_B|} = \frac{F_s\cdot\eta}{8}\cdot J \tag{6}$$

The above derivation establishes an analytical mapping relationship between the spring's axial thrust and the positive radial pressure at the wheel end, providing a theoretical basis for the subsequent comprehensive design of the mechanism and selection of spring stiffness under variable-diameter operating conditions.

3 Dynamic Analysis of Robot Obstacle Crossing

3.1 Theoretical Analysis of Obstacle Crossing Mechanics

3.1.1 Establishment of a Force Model for Obstacle Crossing

When the drive wheel comes into contact with the raised circumferential weld, it must overcome transient running resistance and prevent longitudinal slippage. The umbrella-shaped link support mechanism used in this paper possesses a certain capacity for force compensation: the radial displacement caused by a single wheel overcoming an obstacle can be converted by the links into compression of the central spring, which helps reduce mechanical shock. Therefore, the transient dynamics of the obstacle-crossing process can be simplified to a quasi-static model for analysis[24].

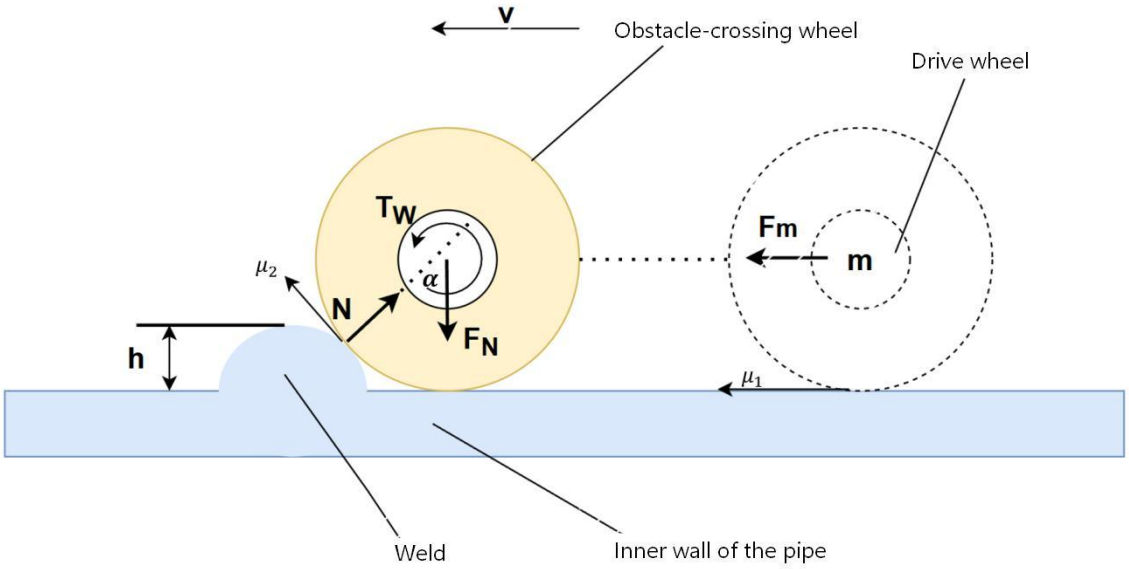


Fig. 3 Force analysis diagram of the drive wheel when crossing an obstacle

To simplify the calculations, the following reasonable assumptions are made: (1) Local plane assumption: The effect of pipe wall curvature is neglected, and the contact area between the wheel and the weld is treated as a plane rolling model; (2) Regular geometry assumption: The irregular cross-sectional contour of the circumferential weld is simplified to a standard semicylinder; (3) Ideal rigid body assumption: The viscoelastic damping of the wheel tread and the mechanical friction damping are neglected to analyze the force boundaries under limit conditions.

The quasi-static analysis method is a classical approach for evaluating the obstacle-crossing limit of wheeled pipeline robots, which has been widely verified in relevant research[14]. Based on the above assumptions, geometric and mechanical analysis models are established for the drive wheel under obstacle-crossing working conditions. The instantaneous state where the obstacle-crossing wheel just lifts off the pipe wall is analyzed, and the corresponding schematic diagram is drawn as shown in Figure 3. The relevant parameters are defined as follows: r denotes the radius of the drive wheel; h represents the height of the obstacle step; T_w is the driving torque of the obstacle-crossing wheel; F_N is the normal compression force acting on the wheel center; N stands for the force exerted by the circumferential weld on the wheel; α is the obstacle-crossing angle; F_m refers to the cooperative force on the same wheel axis, where m is the number of cooperative wheels on one axis; μ_1 is the friction coefficient between the drive wheel and the inner pipe wall, and μ_2 is the friction coefficient between the drive wheel and the circumferential weld.

3.1.2 Traction Boundary Analysis

A prerequisite for a drive wheel to clear an obstacle is sufficient traction torque. In a distributed drive architecture consisting of three short sections connected in series, when a drive wheel clears an obstacle, the power required to do so is provided not only by its own drive motor but also by the axial cooperative thrust from the drive wheel assembly located behind it on the level section of track.

Establish the torque balance equation using point P—the point of contact between the drive wheel and the weld—as the fulcrum. At the critical state of obstacle crossing, the torque balance equation for the drive wheel is:

$$T_w + F_m(r-h) = F_N\sqrt{2rh-h^2} \tag{7}$$

Square both sides of the equation and simplify it into a standard quadratic equation in the variable h:

$$(F_m^2 + F_N^2)h^2 - 2\left(F_m(T_w + F_m r) + rF_N^2\right)h + (T_w + F_m r)^2 = 0 \tag{8}$$

3.1.3 Analysis of Anti-Slip Adhesion Boundaries

Provided that the traction torque requirement is met, the obstacle-crossing capability of the drive wheels is limited by the friction and adhesion conditions at the contact surface between the wheels and the obstacle. Given that the surface roughness of circumferential welds in actual pipelines is typically greater than that of smooth pipe walls, a differentiated friction mechanics model is adopted here.

By orthogonally decomposing the forces acting on the drive wheel into horizontal and vertical components, the system of static equilibrium equations under the ultimate limit state is established as follows:

$$\begin{cases} N\cos\alpha + \mu_2 N\sin\alpha - F_N = 0 \\ m\mu_1 F_N + \mu_2 N\cos\alpha - N\sin\alpha = 0 \end{cases} \tag{9}$$

By solving the system of two equations, we can derive an analytical expression for the tangent of the contact angle that accounts for heterogeneous friction coefficients.

$$\tan\alpha_{\max} = \frac{m\mu_1 + \mu_2}{1 - m\mu_1\mu_2} \tag{10}$$

Combining the geometric constraints, we derive the forward solution formula for the maximum obstacle-crossing height under heterogeneous adhesion constraints:

$$h_{f\max} = r\left(1 - \frac{1}{\sqrt{1 + \left(\frac{m\mu_1 + \mu_2}{1 - m\mu_1\mu_2}\right)^2}}\right) \tag{11}$$

Parameters are selected according to the actual structure of the robot and pipeline operating conditions: r = 0.075 m, m = 2, μ_1 = 0.4, μ_2 = 0.45. The actual maximum obstacle-crossing height of the robot is determined by the minimum value among the dual boundary constraints.

$$h_a = \min(h_{T\max}, h_{f\max}) = \min(50.5\text{mm}, 36.6\text{mm}) = 36.6\text{mm}$$

3.1.4 Calculating the Maximum Obstacle-Crossing Height

According to the actual robot structure and pipeline operating conditions, the driving wheel radius is set as r=75mm, the coaxial coordinated driving force F_D=1500N, the number of coordinated wheels m=3,$\mu_1 = 0.9, \mu_2 = 0.3$. The actual maximum obstacle-crossing height of the robot is determined by the minimum value within the dual boundary constraints. Substituting the relevant parameters into the above equations for solution reveals that the maximum obstacle-crossing height is mainly limited by the friction adhesion limit at the contact surface between the drive wheel and the weld, with the limit height $h_{max} \approx 8.5$mm.

Referring to the relevant standards for natural gas pipeline engineering[13], the reinforcement height of circumferential welds inside pipelines is generally no more than 6 mm. Theoretical calculations demonstrate that the driving scheme proposed in this paper provides a safety margin of approximately 2.5 mm, which can satisfy the obstacle-crossing and passing requirements for in-line inspection of long-distance transmission pipelines.

3.2 Analysis of Geometric Constraints on Pipe Bending Passability

3.2.1 Analysis of Geometric Constraints in Single-Section Curved Pipes

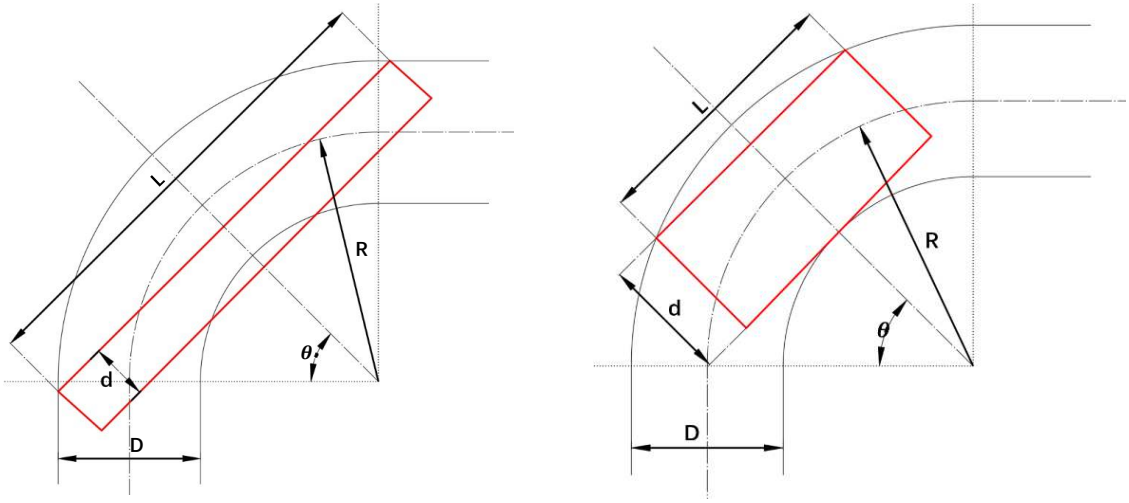
In response to changes in the macro-pipeline network layout—particularly the 5D bends in the DN1016 main line—the robot's axial dimensions and flexible deformation capabilities must meet specific geometric constraints. Since the robot consists of multiple short rigid sections connected in series via universal joints, the rigid body generates a "chord effect" when entering a curved pipe. If a single section of the body is too long or the articulation parameters between the short sections are improperly configured, geometric interference with the inner wall of the bend is likely to occur, resulting in operational jamming.

To ensure the robot's ability to navigate through bent pipes, a geometric interference analysis must be performed. This section establishes a geometric model for the robot's ability to navigate through bent pipes: based on the navigability conditions for a single-segment body, the maximum allowable length of the single-segment body under interference-free conditions is calculated[11].

In the geometric analysis of a single-section robot arm passing through a bent pipe, there are two typical operating conditions regarding the relative position of the robot arm and the pipe wall: (1) the transition condition, in which, as the robot arm enters and exits the bent pipe, its two ends are located within the straight pipe sections on either side of the bend; (2) the steady-state bending condition, in which the entire robot arm is completely within the curved section of the pipe. To prevent geometric interference during the robot's passage through the bend, it is necessary to analyze the constraints between the robot's dimensions and the geometric parameters of the bend.

The system is equivalently simplified considering the extreme geometric constraints: it is assumed that

the adaptive supporting wheels are squeezed by the pipe wall to reach the ultimate compression state, and each single-section body is equivalent to a rigid cylinder with the maximum outer contour dimension. In the 2D planar projection, this equivalent cylinder is simplified into a rectangle with length L and width d. Let the inner diameter of the pipeline be D, the curvature radius of the bent pipe be R, and the central angle of the bent pipe be 2θ. On this premise, the uneven pipe wall thickness and local elastic deformation are neglected, and a geometric constraint model is established with the curvature center of the bent pipe as the origin, as shown in Figure 4. By analyzing the critical tangency conditions under the above two working conditions, the maximum dimensional boundary for the robot body to pass through the bent pipe without interference is solved.



（1）Transient Operating Condition　　（2）Steady-State Bend Negotiation Condition

Fig. 4 Geometric analysis diagram of single fuselage passing through a bend

When the robot is in a transition state inside a bent pipe—that is, when both ends of its body are located within straight pipe sections:

$$0 < d < \left(R + \frac{D}{2}\right)\cos\theta - \left(R - \frac{D}{2}\right) \tag{12}$$

Similarly, when the robot is in a steady-state turning condition inside the curved pipe—that is, when the entire robot body is completely within the curved section of the pipe:

$$\left(R + \frac{D}{2}\right)\cos\theta - \left(R - \frac{D}{2}\right) < d < D \tag{13}$$

Based on the geometric relationship for a robot entering a pipe:

$$\left(\frac{L}{2}\right)^2 + \left(R - \frac{D}{2} + d\right)^2 = \left(R + \frac{D}{2}\right)^2 \tag{14}$$

Substituting Equation (14) into Equations (12) and (13), respectively, yields the maximum length dimensions for the robot under the two operating conditions:

$$\begin{aligned} L_{1max} &= 2\left[\left(R + \frac{D}{2}\right)\sin\theta + \left[\left(R + \frac{D}{2}\right)\cos\theta - \left(R - \frac{D}{2} + d\right)\right]\cot\theta\right] \\ L_{2max} &= 2\sqrt{\left(R + \frac{D}{2}\right)^2 - \left(R - \frac{D}{2} + d\right)^2} \end{aligned} \tag{15}$$

The above equations describe the basic geometric constraints for a robot to pass through a curved pipe without interference. Given that the internal inspection robot designed in this paper employs a configuration consisting of multiple short sections connected in series, and in order to balance internal payload capacity with operational maneuverability, this section performs a geometric boundary check on a single-section body under steady-state bend traversal conditions.

The robot is adaptable to pipelines with inner diameters ranging from 910mm≤D≤1030mm, and the

central curvature radius of the 5D bent pipe is R=5080mm. Let d denote the equivalent rigid width of the robot body under the ultimate compression state inside the pipeline. For verification under extreme working conditions, the outer contour diameter of the diameter-variable mechanism at its minimum contraction state $d = 910mm$ is adopted for calculation. Substituting the above parameters into the equations yields the maximum allowable length of a single robot section: $L \leq 1488mm$.

The actual axial length of the single-section body designed in this paper is 1450 mm, which satisfies the above geometric constraints for passing through bent pipes. The calculated value of 1488 mm represents the limit wheelbase constrained by the front and rear suspension wheel assemblies. In the actual structure, the diameter of the middle sealed cabin is smaller than the outer contour width of the suspension, resulting in a relatively large radial clearance inside the bent pipe with a certain safety margin. Therefore, in the comprehensive structural dimension design phase, only the wheelbase between the front and rear wheel sets of each single-section body needs to be controlled within the safe range. The slender feature of the middle cabin can avoid geometric interference in the central part, guaranteeing the robot's bidirectional passage capability inside 5D bent pipes.

3.2.2 Geometric Constraint Analysis of Geometric Constraint Analysis for Bend Traversal of Multi-Section Series-Connected Robots

Based on the calculations of the maximum dimensions of a single-segment robot body in the previous section, this section further explores the coupled motion characteristics of a multi-segment robot in a 5D curved pipe. Compared to the independent bend traversal, a system consisting of segments connected in series via universal joints exhibits motion coupling effects when navigating a bend, as the positions and orientations of the front and rear segments are subject to the geometric constraints of the connecting mechanism. Although the robot designed in this paper features a three-segment configuration, given the repetitive nature of the system's structure, analyzing a subsystem consisting of two adjacent segments and their connecting universal joints is sufficient to characterize the geometric behavior of the entire robot during bend traversal.

Under the multi-section bend-passing condition, the effective length L_{u} of the universal joint is a critical parameter affecting the system's passability, and its value range is restricted by the following two geometric interference boundaries:

(1) Inner wall interference boundary: If the universal joint length L_{u} exceeds the critical upper limit, the connecting mechanism will span the inner side of the bent pipe during bending negotiation. Its middle section is prone to interference and friction with the inner wall of the bent pipe, thereby bringing hidden dangers to operation safety.

（2）End-face interference boundary: If the universal joint length L_{u} is less than the critical lower limit, the front and rear sections will draw close to each other under the curvature effect of the bent pipe when passing the bend. The end faces of adjacent body sections are likely to collide and interfere, resulting in system jamming.

In summary, the universal joint length L_{u} must fall within an effective dimensional interval that avoids both inner wall interference and end-face interference. To establish an equivalent mathematical model and solve for this interval, reasonable simplification assumptions are proposed for the physical system as follows:

（1）Rigid body assumption: Elastic deformation of the universal joint and connecting base is neglected, and they are equivalent to a rigid connecting rod linking the geometric centers of the front and rear sections.

（2）Coplanar and coincident axis assumption: It is assumed that under the action of the supporting mechanism, the central axes of the front and rear sections always coincide with the geometric centerline of the pipeline, and all motion axes lie within the 2D projection plane of the bent pipe.

（3）Single-section passability assumption: The geometric dimensions of each single body section are assumed to satisfy the single-section passability conditions derived in the previous section, and single-module interference is not taken as a variable in the coupled equations established herein.

For the working condition of the inner wall interference boundary, a geometric model as shown in Figure 5 is built to solve the maximum allowable length of the universal joint when the robot passes through the bent pipe without interference.

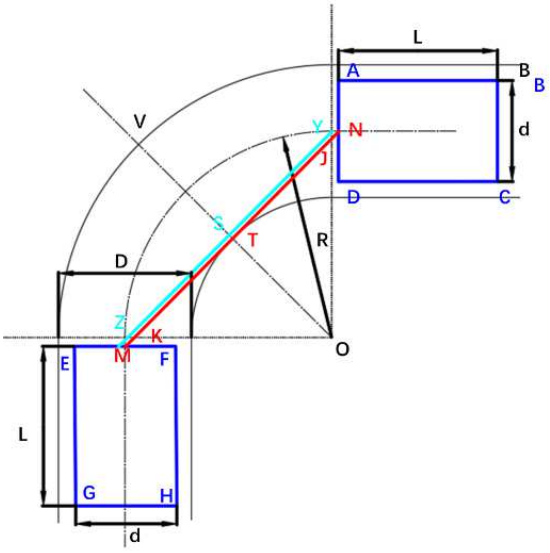


Fig. 5 Geometric constraint diagram under the interference boundary of multi-section bending inner wall

In this model, points M and N are defined as the hinge centers connecting the universal joint with the front and rear sections respectively, and point T denotes the critical contact point where the middle segment of the universal joint is tangent to the inner wall of the bent pipe. Based on the above geometric relations, the calculation formula for the maximum allowable length $L_{u\max}$ of the universal joint is derived as follows:

$$\begin{aligned} L_{u\max} &= \mathrm{MN} < \mathrm{MK} + \mathrm{KJ} + \mathrm{JN} \\ &= \mathrm{MK} + \mathrm{KT} + \mathrm{TJ} + \mathrm{JN} \\ &= 2\times MK + 2\times OT \end{aligned} \tag{16}$$

In the geometric diagram, △ZMK can be shown to be an equilateral right triangle, so we can conclude that:

$$\begin{cases} ZM = ZK = l \\ MK = \sqrt{2\times MZ^2} \end{cases} \tag{17}$$

In the formula, l denotes the distance at which the first section of the robot exits the bent pipe. Since both △ZOY and △KOJ are isosceles right triangles, we can obtain:

$$\begin{aligned} \mathrm{ZK} &= \mathrm{OZ} - \mathrm{OK} \\ &= OZ - OT/\cos\theta \\ &= R - (R - D/2)/\cos\theta \end{aligned} \tag{18}$$

Therefore, the maximum allowable length of the universal joint $L_{u\max}$ is expressed as:

$$\begin{aligned} L_{u\max} &= MN < 2\times MK + 2\times OT \\ &= 2\sqrt{2\times ZK^2} + 2\times OT \\ &= 2\sqrt{2\times\left(R - (R - D/2)/\cos\theta\right)^2} + 2\left(R - D/2\right) \end{aligned} \tag{19}$$

As can be seen from this equation, the maximum allowable length of the universal joint depends on the inner diameter of the pipe and the radius of curvature of the bend.

For end-face interference boundary conditions, a geometric model as shown in Figure 6 was established to determine the minimum allowable length of the universal joint that prevents end-face interference between adjacent short sections as the robot navigates the bend.

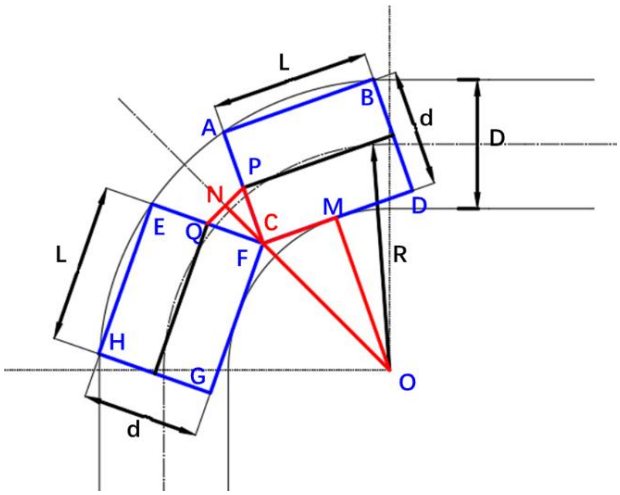


Fig. 6 Geometric constraint diagram under the interference boundary of multi-section curved end face

Where point N is the midpoint of the universal joint segment PQ, and point M is the tangent contact point between the rear module of the robot and the inner wall of the bent pipe, as well as the midpoint of segment CD. It can be seen from the geometric relation diagram that △OCM and △CNP are right triangles. We can obtain:

$$\frac{NP}{MC} = \frac{CP}{OC} \tag{20}$$

In △OCM, we have:

$$\begin{cases} ON = R \\ CM = L/2 \\ OC = \sqrt{(OM)^2 + (MC)^2} \end{cases} \tag{21}$$

Substituting the parameters yields the minimum allowable length L_{umin} of the universal joint:

$$L_{u\max} = PQ > 2NP = \frac{dL}{\sqrt{4R^2 + L^2}} \tag{22}$$

Combining the geometric constraint models for inner wall interference and end-face interference above, the structural parameters of the target pipeline and single-section body are substituted for calculation. To avoid interference between multiple sections inside the bent pipe, the allowable length range of the universal joint is calculated as $132mm \leq L_u \leq 4911mm$.

The central hinge length of the universal joint designed in this paper is 183 mm, which falls within the theoretical safe interval and verifies the rationality of parameter design. On the one hand, the axial spacing of 183 mm exceeds the critical lower limit for end-face interference, reserving a certain spatial margin for the pose deflection of front and rear sections inside 5D bent pipes. On the other hand, this dimension is smaller than the theoretical upper length limit for inner wall interference, which helps improve the overall stiffness and axial compactness of the multi-body series system.

3.3 Bend Passability Analysis of the Robot

Long-distance natural gas pipelines include bends designed to accommodate thermal deformation and route adjustments. To verify whether the designed three-segment series pipeline robot can navigate a 5D bend without experiencing motion jamming or geometric interference, a dynamic bend-navigation simulation must be conducted. In this section, based on the geometric passability conditions established earlier, a virtual prototype model of the robot is constructed in the ADAMS multibody dynamics software [26–28]. By simulating the dynamic response during curve navigation under rated operating conditions, the system's trajectory-following capability and the pose deviation characteristics of the universal joints are analyzed.

3.3.1 Model Development and Parameter Configuration

To balance solution efficiency and computational accuracy, the robot's 3D model was geometrically cleaned up by removing non-critical features that had minimal impact on the kinematic analysis, after which it was imported into multibody dynamics simulation software. At the same time, a 90° bent pipe model with a radius of curvature R = 5D was constructed in the simulation environment. Based on the robot's kinematic structure, universal joint pairs were defined between the three short segments—the head, middle, and tail—to provide the spatial deflection degrees of freedom required for turning. Corresponding fixed joints and constrained joints were applied according to the actual assembly relationships. The simulation model is shown in Figure 7.

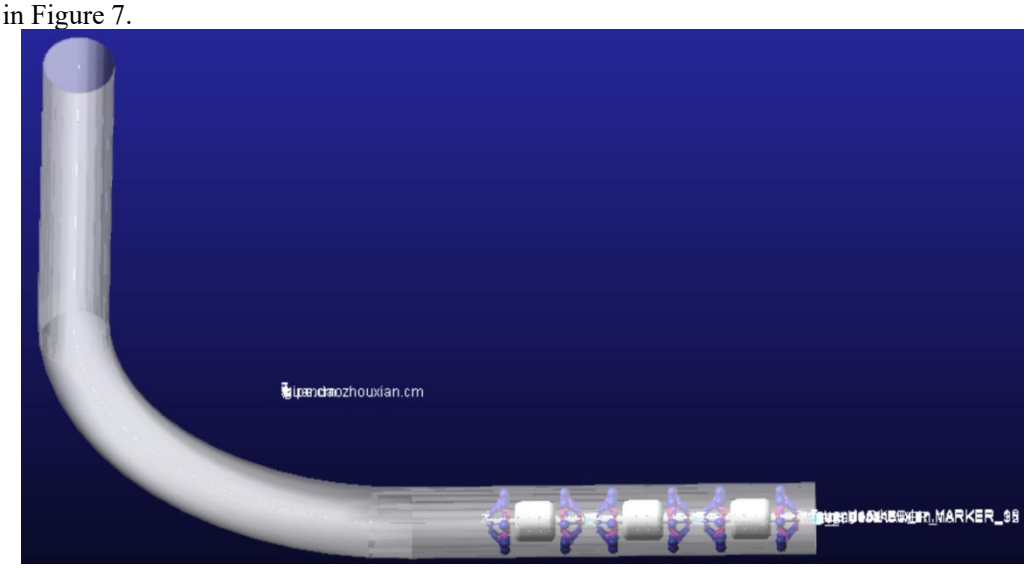
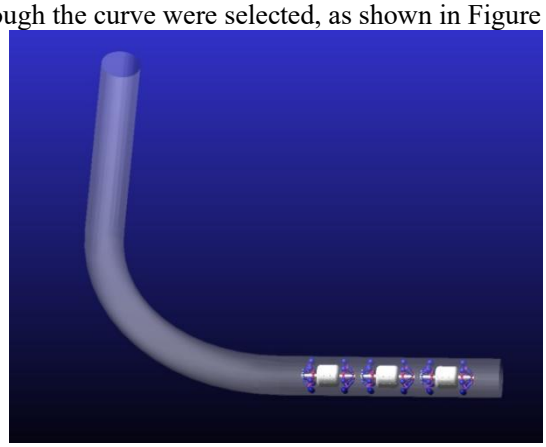


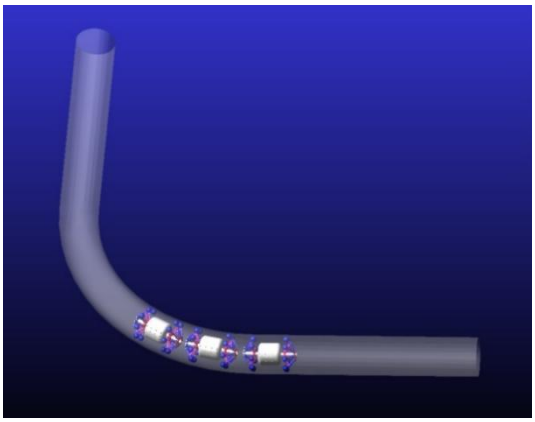
Fig. 7 Virtual prototype model of pipeline robot

To simulate the robot's operating state and solve contact force characteristics, a constant velocity driving constraint of 1m/s is applied to the driving components. Meanwhile, the total simulation duration is set to 15s with 5000 simulation steps. This parameter setup can cover the complete operation cycle of the robot consisting of "straight pipe – bent pipe – straight pipe", and satisfy the calculation accuracy requirements for dynamic response curves.

3.3.2 Analysis of Sexual Simulation Results

To analyze the geometric interference and pose coordination of the robot inside the curved pipe, motion state diagrams were extracted from the simulation process. Four typical moments during the robot's passage through the curve were selected, as shown in Figure 8.





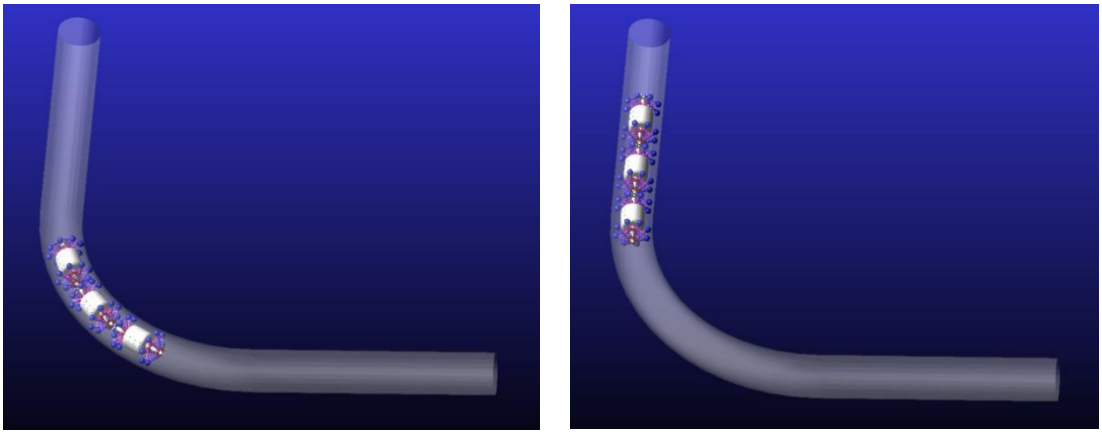


Fig. 8 Motion simulation process of robot through a bend

As shown in the motion pose diagram for navigating the bend, the robot utilized the spatial deflection degrees of freedom of the universal joint to pass through the 90° bend without any end-face interference or movement jamming between adjacent short sections. To further quantitatively analyze its ability to navigate the bend, the following analysis examines three dimensions: spatial motion trajectory, universal joint pose, and dynamic response.

(1) Spatial Trajectory and Joint Pose Response

To verify the robot's trajectory-following performance inside the pipe, the spatial position change curves of the centers of mass for the first, middle, and last short sections were extracted over the entire simulation cycle.

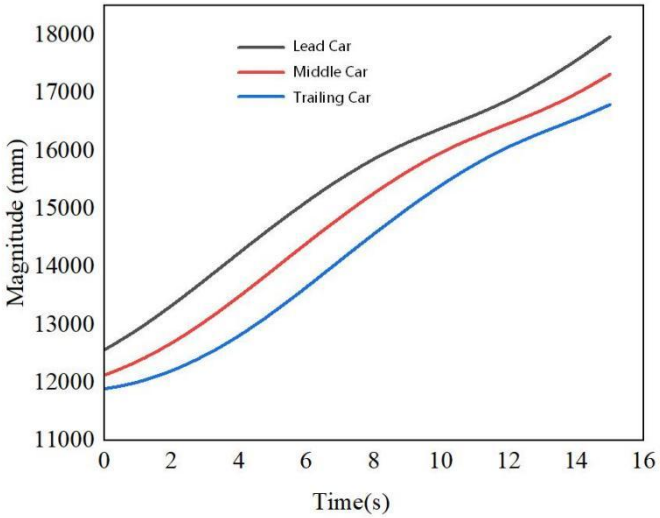


Fig. 9 The spatial position change curve of the three short section centroids of the robot.

As shown in Figure 9, the combined displacement of the three short sections exhibits a largely consistent trend over the 15-second simulation cycle, with the curve as a whole displaying a smooth, nonlinear, and monotonically increasing pattern. No steps or abrupt changes occurred in the displacement curve throughout the entire cycle; the slope of this continuous change reflects the robot's dynamic operation as it enters the 90° elbow from the front straight pipe section and eventually exits into the rear straight pipe section.

Building on the verification of the trajectory-following characteristics, it is necessary to further analyze the deflection angles of the articulated joints in each short section to verify whether the system is prone to motion jamming. To this end, the deflection angle response curves of the front and rear universal joints throughout the entire simulation cycle were extracted, as shown in Figure 10.

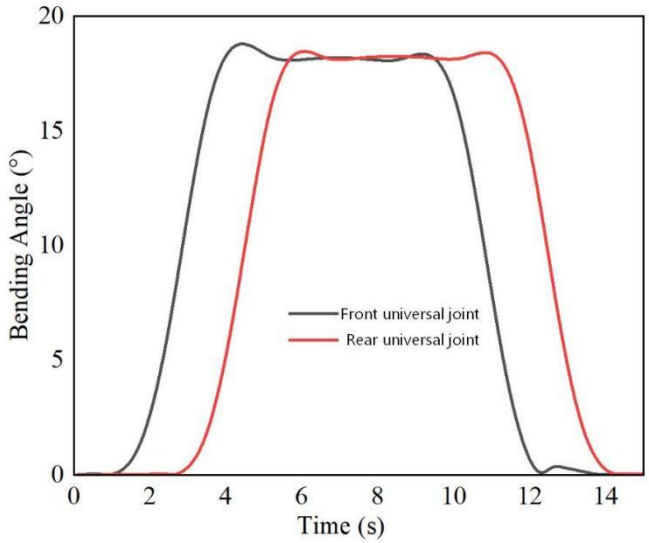


Fig. 10 The curve of the deflection angle of the universal joint before and after the robot changes with time.

As can be seen from the deflection angle curves of the universal joints, due to the motion characteristics of the multi-link series mechanism, the deflection angle curves of the front and rear universal joints exhibit a phase difference related to the wheelbase of the short links, reflecting the system's dynamic sequence of "the front short link entering the turn, the entire system passing through the turn in a steady state, and the rear short link exiting the turn."

From the extreme values of the deflection angles, it can be seen that when the entire robot enters the arc segment and is in a steady-state cornering condition, the deflection angles of both the front and rear universal joints stabilize at around 18.5°, and the curve exhibits a symmetrical, smooth trapezoidal region. The deflection limit of the cross-axis universal joint lies between 35° and 45°. This peak angle of 18.5° indicates that, under pipe-bending conditions with R = 5D, the connecting mechanism—with its current dimensional configuration—possesses a safety margin of over 50% in terms of deflection angle. This prevents joint interference and motion jamming within confined spaces and also provides the robot with a certain degree of adaptability when navigating non-standard pipe fittings.

(2) Speed Tracking and Dynamic Response Analysis

Based on the verification of the kinematic interference-free characteristics, it is necessary to further analyze the operational smoothness of the mechanism under cornering contact conditions. The dynamic velocity response curves of the centers of mass of the front, middle, and rear short segments under the specified drive conditions are shown in Figure 11.

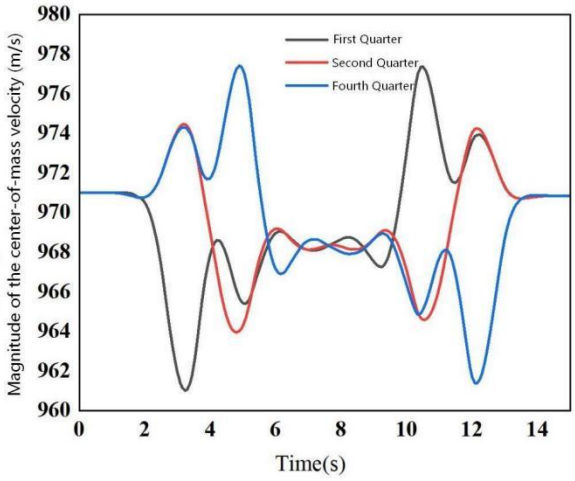


Fig. 11 The velocity response curve of the robot 's bending centroid

As shown in Figure 11, the drive speed set at the front end of the system is 1000 mm/s. During steady-state operation in the straight pipe section, the actual center-of-mass velocity of the three short sections stabilizes at around 970 mm/s. This steady-state velocity difference of approximately 3% reflects the longitudinal slippage generated by the multibody system as it overcomes pipe wall friction and universal joint damping, thereby validating the validity of the dynamic model.

Throughout the entire cycle of passing through a 90° bend, the system's velocity evolution exhibits nonlinear characteristics: when the lead section enters the curved section of the bend, an instantaneous deceleration occurs due to increased running resistance; due to the geometric relationships during the bend, the middle and trailing sections compensate for the motion under the traction of the universal joint, resulting in a localized acceleration response. As the entire system fully enters the curved section, the velocities of the three segments tend to converge due to the contact between the pipe walls, oscillating slightly around 968 mm/s. This steady-state turning velocity is slightly lower than that in the straight section, consistent with the mechanical principle that turning resistance exceeds running resistance in straight sections. Subsequently, as the leading section exits the curved pipe and enters the rear straight section, the reduction in steering resistance causes its speed to rebound; at this point, the trailing section remains within the curved pipe and is subjected to significant running resistance, resulting in a lagging minimum in its speed. Finally, after 14 seconds, the system's overall speed steadily returns to the straight-pipe running speed of approximately 970 mm/s.

As shown by the velocity response curve, although there are local velocity fluctuations and transient velocity differences between the short sections when entering and exiting the curved section, the trends in velocity changes across the short sections are generally consistent, and the overall fluctuation amplitude is controlled within ±1%. The system did not exhibit significant deceleration or severe longitudinal oscillations, confirming that the multi-section series mechanism possesses good longitudinal power transmission and motion tracking performance under bend traversal conditions.

(3) Analysis of Transient Angular Acceleration

Nonlinear changes in velocity cause a redistribution of contact forces within the system. During bend traversal of multi-segment series robots, the transient angular acceleration of the segments about spatial axes better reflects the steering impact and joint torsional loads at the curvature transition between straight and curved pipes than linear acceleration, which includes a centripetal component. To this end, the transient angular acceleration curves of the centers of mass of the three segments were extracted, as shown in Figure 12.

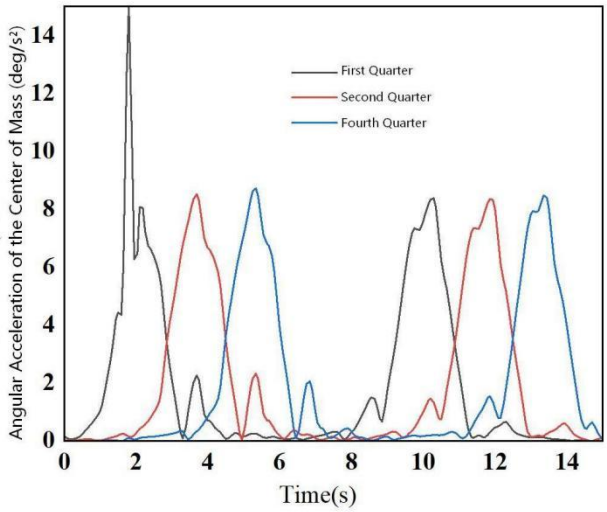


Fig. 12 The angular acceleration response curve of the robot 's bending centroid

As shown in Figure 12, the system's angular acceleration response curve reflects the transient steering shock caused by sudden changes in pipe wall curvature within a confined space. During the steady-state bend traversal phase in the leading and trailing straight pipe sections and when fully entering the arc, the angular accelerations of the three short sections remain at relatively low levels because the system's yaw angular velocity tends toward a constant value or zero. However, during the transition phases at the entrance and exit of the curve, due to a sudden change in the spatial steering angular velocity, the three short sections generate peak angular accelerations in sequence, following a phase lag order related to their axial distances. The analysis results indicate that the leading section, which enters the curved pipe first, experiences a significant transient steering impact, with a peak angular acceleration of approximately 15 deg/s²; due to the deflection and damping effects of the universal joint mechanism, the peak angular accelerations of the subsequent middle and trailing sections decrease to approximately 8.5 deg/s², representing a reduction of about 43%.

This characteristic of gradually decreasing angular acceleration indicates that the multi-segment series-connected chassis structure can reduce the transient torsional impact generated when traversing a bend at a

speed of 1,000 mm/s and possesses a certain degree of cushioning and damping capability, thereby verifying the robot's operational stability in three-dimensional bends within long-distance pipeline networks.

3.4 Multibody Dynamics Simulation Analysis of Obstacle Crossing

3.4.1 Development of the Simulation Model

Considering that the original vehicle chassis is equipped with 48 support wheels, introducing all wheel assemblies into a multibody dynamics simulation for contact and **collision** analysis can easily lead to numerical oscillations in transient contact forces, which in turn can cause the solver to fail to converge. Therefore, this paper performs a dynamic equivalence simplification of the chassis wheel system, reducing it to a kinematic framework consisting of "three sets of drive wheels in the front row and three sets of support wheels in the rear row." The simplification process follows the principles of "equivalence of mass and inertia" and "invariability of single-wheel force boundaries." The preload of the central spring is reduced in proportion to the wheel set reduction ratio to ensure that the normal compression force on a single wheel matches that under actual full-load conditions. While preserving the chassis's wheelbase characteristics and primary kinematic relationships, this equivalent model reduces the computational resources required by the contact-collision algorithm and provides a modeling foundation for subsequently extracting transient dynamic data during obstacle crossing. The obstacle-crossing model is shown in Figure 13.

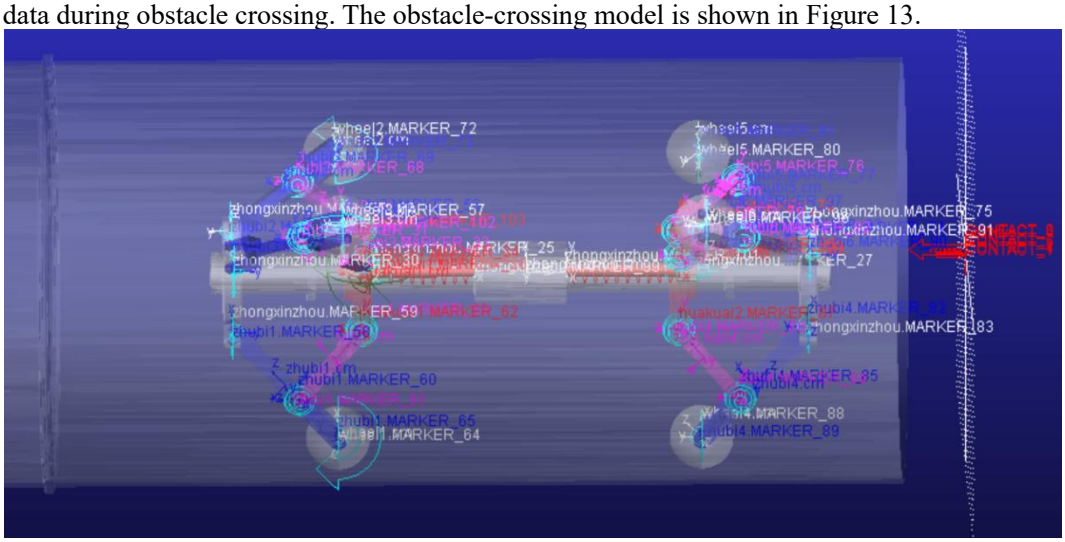


Fig. 13 The constraint relation diagram of robot obstacle crossing model

3.4.2 Simulation Parameter Settings

Taking into account the contact and collision characteristics during obstacle crossing and actual operating conditions, the mechanical contact parameters between the wheels and the pipe wall, as well as the boundary conditions for the drive joints, were configured to prevent oscillations in the contact force values and to simulate the soft-start characteristics of the drive motor. The simulation parameters and drive functions are shown in Table 2.

Table2 Robot obstacle simulation parameter setting

Parameter Category	Variable Name	Set Value
Contact Parameters	Contact Stiffness (K)	30000N/nm
	Impact Exponent (e)	1.5
	Damping Coefficient (C)	30N · s/mm
	Penetration Depth (d)	0.1mm
Friction	Static Friction Coefficient	0.6
	Dynamic Friction Coefficient	0.4
	Static Transition Velocity	1.0
	Friction Transition Velocity	10.0
Drive Boundary	Driving Function	STEP(time, 0,0,0.5,746d)

3.4.3 Analysis of Obstacle-Clearing Dynamic Responses at Different Speeds

To analyze the geometric interference and pose coordination of the robot during obstacle crossing, motion state diagrams were extracted from the simulation process. Two typical moments during the robot's obstacle crossing were captured, as shown in Figure 14.

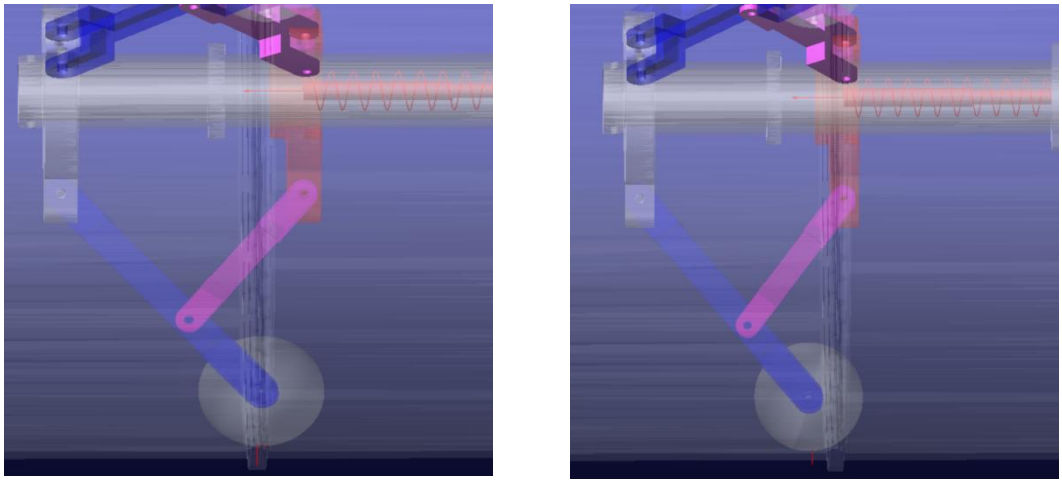


Fig. 14 Motion simulation process of robot crossing obstacles

The simulation animation shows that the entire obstacle-crossing process is very smooth. To further evaluate the dynamic response of the chassis structure when crossing a 6-mm circumferential weld and to provide a basis for determining a reasonable operating speed, this paper conducted a parametric simulation analysis within the speed range of 0.12 m/s to 1.2 m/s. By extracting the maximum torque of the drive wheels and the maximum vertical displacement of the center of mass during the obstacle-crossing process, we obtained the curves showing how the peak dynamic response varies with drive speed, as shown in Figure 15.

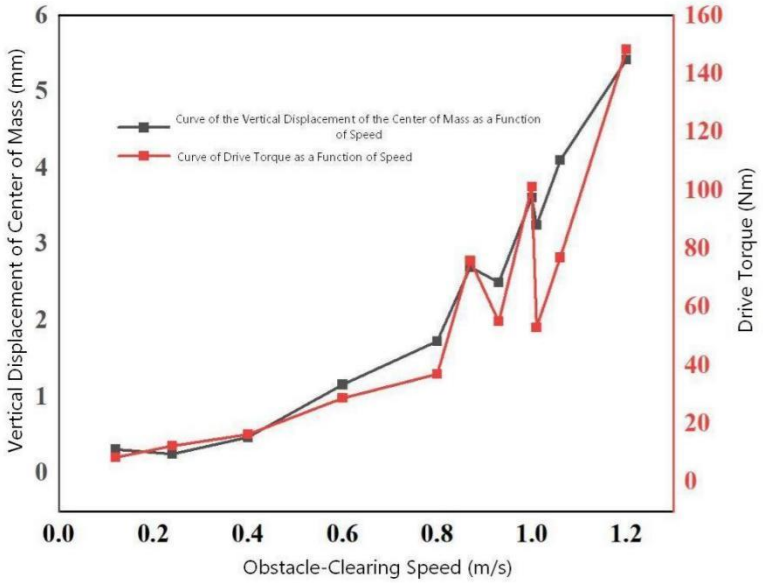


Fig. 15 Transient dynamic response characteristic curves of the robot at different obstacle-crossing speeds.

As shown in Figure 15, the system's dynamic response exhibits a piecewise nonlinear behavior. When the obstacle-crossing speed exceeds 0.6 m/s, the peak drive torque and the vertical displacement of the center of mass increase rapidly due to the increased kinetic energy resulting from contact and collisions. When the speed drops below 0.4 m/s, the amplitudes of the drive torque and the center of mass displacement decrease significantly and tend to level off.

Furthermore, the system's dynamic response in the higher-speed range does not follow a monotonically increasing pattern. As shown in the figure, near 1.0 m/s, both the drive torque and the vertical displacement of the center of mass reach local peaks; when the obstacle-crossing speed increases slightly, these peak loads begin to decline. This nonlinear abrupt change may be related to the dynamic transition effect generated when the wheels clear obstacles at higher speeds; that is, due to significant normal kinetic energy, the wheels partially cross the weld seam contour, thereby reducing the actual contact force. Although this dynamic characteristic can reduce transient obstacle-clearing resistance under specific conditions, its trigger threshold is highly sensitive to speed and is subject to uncertainty in actual pipeline network operating conditions. To ensure the stability and safety of pipeline inspection operations, the obstacle-crossing speed should be controlled within a reasonable range of 0.4 m/s or less.

Taking into account both the maximum torque threshold of 25 Nm for the motor shown in the figure and the operational stability of the chassis, this paper selects 0.24 m/s as the robot's rated obstacle-crossing speed, at which the obstacle-crossing torque and changes in the center of mass are minimal. This dynamic response analysis provides a parametric basis for evaluating the system's obstacle-crossing performance and formulating a "speed reduction upon encountering an obstacle" control strategy.

3.4.4 Comparison of High- and Low-Speed Operating Conditions and Determination of Rated Speed

Based on the variation patterns of the dynamic responses described above, to further analyze the contact and collision characteristics during the obstacle-crossing process, two typical conditions—0.24 m/s and 0.93 m/s—were selected, representing decelerated obstacle crossing and full-speed operation, respectively. The displacement domain curves for the entire obstacle-crossing cycle were extracted for analysis. The transient torque curve of the drive wheel is shown in Figure 16.

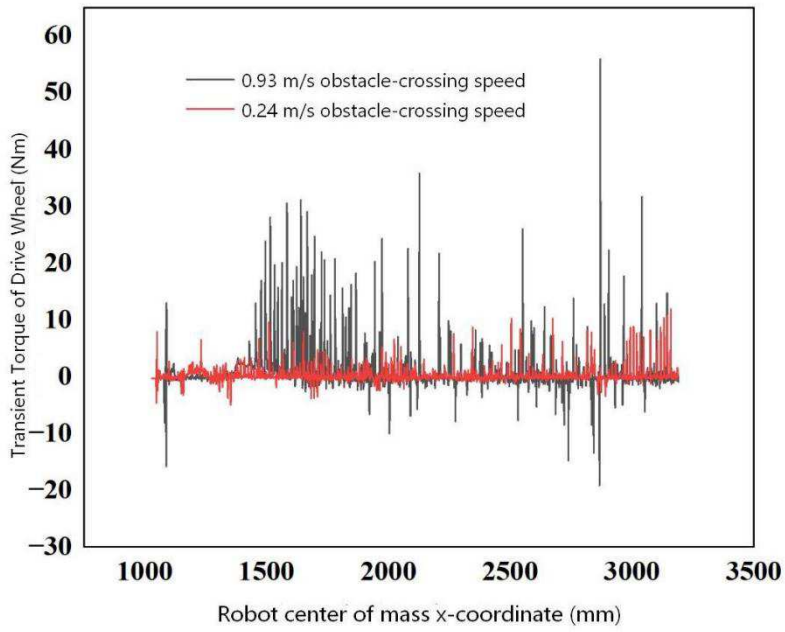


Fig. 16 Comparison curve of transient torque response of obstacle-crossing driving wheel under high and low speed conditions

As can be seen from the comparison of the curves, under operating conditions of 0.93 m/s, there is a distinct high-frequency contact oscillation in the torque response. The maximum torque peak under these conditions is approximately 55 N·m; it does not occur when the drive wheel crosses the step, but rather at the instant the rear support wheel makes contact with the step. This phenomenon indicates that when the rear wheels cross the step, the resulting rolling resistance must be overcome by additional traction provided by the front wheels; combined with the dynamic axle load transfer during obstacle crossing, this causes the drive motor to experience a significant torque peak while propelling the rear wheels over the obstacle.

In contrast, under the rated obstacle-crossing condition of 0.24 m/s, the torque oscillations caused by contact and impact were significantly reduced, with a maximum torque peak of 12.4 N·m. This value falls within the motor's rated load capacity and maintains a safety factor of approximately 2.0 for the robot's operation under actual pipeline conditions, such as oil contamination and incline climbing.

Furthermore, the central spindle, which carries the detection instruments, is relatively sensitive to vibrations. Figure 17 further illustrates the vertical displacement curves of the center of mass for the short section during obstacle crossing under the two sets of operating conditions.

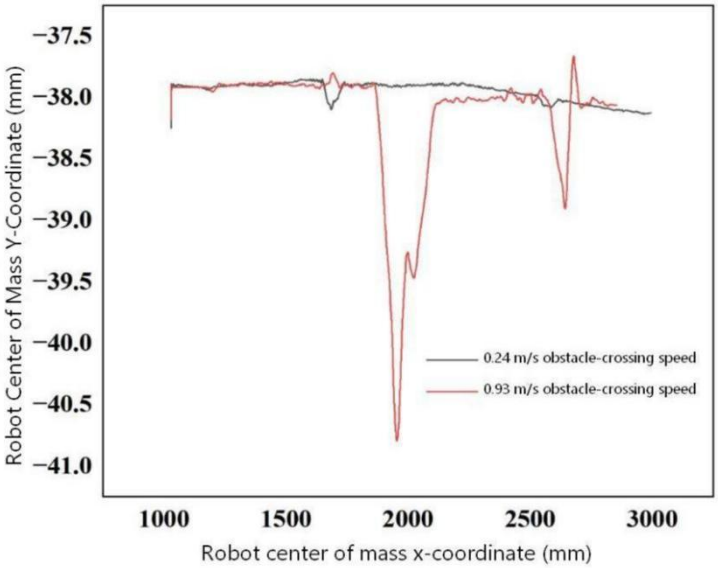


Fig. 17 Comparison of the trajectory of the robot's center of mass under high and low speed obstacle crossing conditions

As shown by the displacement change curve, under operating conditions of 0.93 m/s, the relatively short duration of contact and impact limits the cushioning effect of the chassis suspension system, resulting in a vertical displacement of approximately 3 mm at the center of mass and increasing the risk of damage to the onboard instruments. Under the rated obstacle-crossing conditions of 0.24 m/s, the chassis's adaptive variable-diameter mechanism effectively provides motion damping. The system effectively damps the 6 mm displacement excitation originating from the wheels, limiting the vertical displacement fluctuations of the center of mass to approximately 0.25 mm, with a vibration isolation rate exceeding 95%.

The above analysis of the center of mass response indicates that impact from contact collisions at higher speeds can adversely affect the mechatronic system and the mounting platform, thereby validating the rationality of the robot's control strategy: "high-speed cruising—deceleration upon encountering an obstacle—smooth obstacle crossing."

4 Scaled-Down Model Passability and Obstacle-Crossing Tests

4.1 Setting Up the Experimental Platform

(1) Experimental Platform Setup

To verify the robot's navigability through complex pipeline geometries, this study established an experimental platform consisting of a scaled-down prototype and a simulated pipeline environment.

Following a 1:5 geometric similarity ratio, a proof-of-concept prototype was 3D-printed using PLA material. To eliminate the proof-of-concept prototype's sensitivity to friction-induced disturbances, friction-reduction measures were incorporated: F682W miniature bearings were embedded at all rotating link pairs, and JFB graphite linear bearings were used at the sliding section of the central spindle. Additionally, the return springs for the variable-diameter mechanism were selected based on the principle of equivalent scaled stiffness to ensure that the mechanism's radial support torque matched that under full-scale operating conditions; adjacent short sections were connected using 01GD universal joints.

The test pipeline was constructed using transparent acrylic tubing to facilitate recording the prototype's motion. The experimental pipeline section consisted of a straight pipe with an inner diameter of 194 mm and a 5D bend with a curvature radius of R = 1000 mm; the measured calibration results are shown in Figure 12. A 2-mm-high rigid protrusion was installed at the bottom of the straight pipe section to simulate the misaligned circumferential weld conditions found in real pipelines[29, 30].

(2) Experimental Protocol

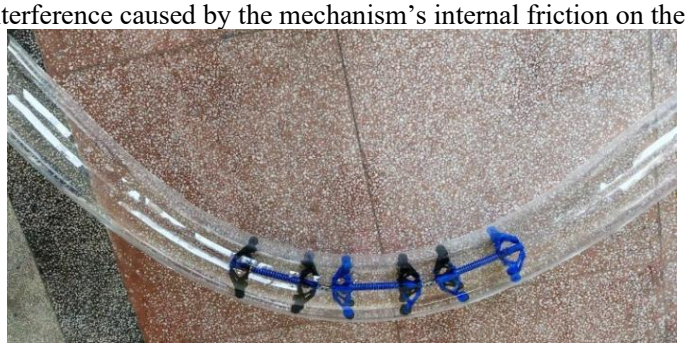
This experiment employs a strategy of controlling variables and step-by-step progression, aiming to determine the force characteristics of the proof-of-concept prototype under complex pipeline geometries. The specific procedure is as follows:

Prior to the start of the experiment, the digital force gauge was zero-calibrated, and the test pipe section was cleaned to maintain a consistent wall friction coefficient. Using the constant-speed traction method, transient traction force values were recorded sequentially as the robot traversed straight pipe sections, circumferential welds, and 5D bends. The mechanism's obstacle-crossing performance and passability were

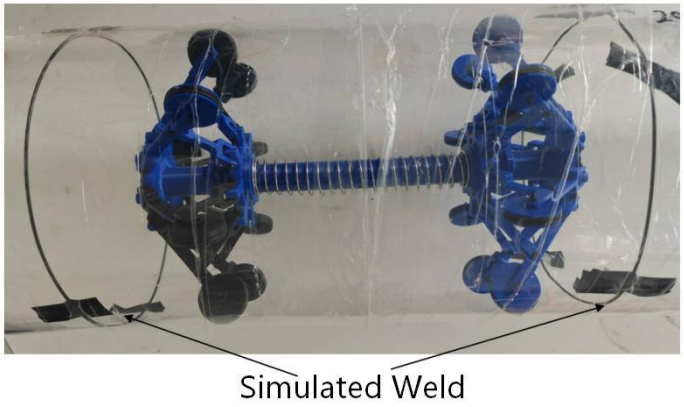
evaluated by comparing the baseline resistance in straight pipe sections with the peak resistance during obstacle-crossing conditions. To minimize random errors, each set of test conditions was repeated five times independently, and the arithmetic mean was taken as the basis for performance evaluation under that condition.

To verify the kinematic feasibility and anti-interference characteristics of the previously designed variable-diameter centering mechanism and series structure within the pipe, a chassis traction test platform was constructed in this section. Taking into account laboratory conditions and 3D printing processes, a 1:5 scaled-down proof-of-concept prototype of the robot chassis was built for this experiment.

To minimize the impact of manufacturing tolerances and surface roughness on the mechanism's motion and ensure the accuracy of the test data, flanged ball bearings were installed at the connecting rod rotating joints, and linear bearings were installed at the sliding points of the central spindle. Additionally, a return spring was installed in the variable-diameter mechanism based on the principle of equivalent scaled stiffness. This design reduces the interference caused by the mechanism's internal friction on the traction force test.



(a) Bend Passability Experiment



(b) Obstacle-Crossing Experiment

Fig. 18 Experimental model of pipeline passing principle

4.2 Pipe Bending Passability Test

In natural gas trunkline operations, pipe bends are sections prone to causing interference with and jamming of internal inspection devices. This section verifies the passage capability and anti-interference characteristics of a series-connected structure through traction experiments conducted on a 1:5 scaled-down prototype in an acrylic 5D pipe bend.

During the experiment, the prototype's maneuvering posture through the bend could be observed through the transparent pipe wall: as the model sequentially passed through the 5D bend, the support wheels remained in close contact with the pipe wall under the action of preload springs. Furthermore, when the modules—connected via universal joints—changed orientation, their internal diameter-adjustment mechanisms maintained effective travel without any mechanical interference or motion deadlock. These observations confirmed that the robot's structural dimensions and variable-diameter stroke met the passability requirements for the 5D bend.

To evaluate the force characteristics of the prototype during pipe bends, the experiment used a digital force gauge to record changes in traction force as the prototype passed through the 5D bend. To address test fluctuations caused by manual traction, the raw force gauge readings were subjected to low-pass filtering and smoothing, which reduced the impact of test interference and allowed for the determination of the prototype's actual traction resistance. The traction force variation curve is shown in Figure 13.

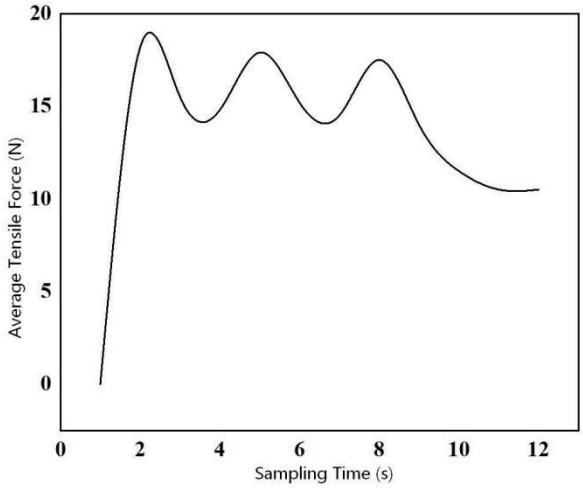


Fig. 19 The change curve of traction force when the model passes through the bend

Analysis of the traction force curve in Figure 19 reveals that, as the model passes through the curved pipe, its traction force exhibits a three-peak fluctuation pattern.

At approximately 2 s, 5 s, and 8 s, the system's traction force reaches peak values of 18.2 N, 17.9 N, and 17.5 N, respectively. This pattern of traction fluctuation is related to the series configuration: as the model's front, middle, and rear modules enter the curved pipe in sequence, changes in attitude deflection and friction cause the system's traction to increase; subsequently, as each module adjusts its attitude via the universal joints, the traction gradually decreases to approximately 15 N. These experimental results validate the curved-pipe passability of the series-connected module configuration and are consistent with the multi-body dynamics simulation results described earlier.

4.3 Circumferential Weld Obstacle-Crossing Test

In natural gas pipeline operations, misalignment of the inner wall caused by welding and circumferential welds are the primary factors leading to vibration or jamming of the detector. To verify the radial yielding capacity and obstacle-crossing feasibility of the chassis' s variable-diameter mechanism, this section conducted rigid obstacle-crossing experiments using a single-section model. Two rigid protrusions, each 2 mm high, were installed within a straight pipe section to simulate misaligned circumferential weld conditions, as shown in Figure 18(b). Analysis of the obstacle-crossing traction force curve in Figure 20 reveals that when the single-section model was cruising along a straight pipe section, its sliding resistance remained stable at around 4.5 N. At sampling times of 4.0 s and 8.0 s—that is, at the moments when the support wheel passed over the rigid protrusions—the system' s traction force fluctuated, reaching peak values of 16.6 N and 17.0 N, respectively.

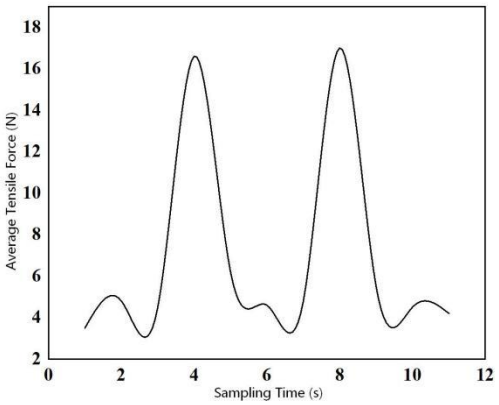


Fig. 20 Traction force change curve of model crossing obstacle

The experimental results show that after reaching its peak, the traction force did not continue to rise or cause jamming; instead, it returned to a level of approximately 5 N within 1 second after clearing the obstacle. This force characteristic demonstrates that the variable-diameter mechanism possesses radial yielding capability. When the system encountered an impact from a rigid protrusion, the normal reaction force acting

on the support wheel drove the central slider to move, causing the main shaft's preload spring to compress and allowing the wheel assembly to contract radially to pass through a 2-mm obstacle. After clearing the obstacle, the spring released its stored energy, driving the support wheel to re-engage with the pipe wall and return to its centered position.

This experiment verified the reliability of the variable-diameter mechanism in handling radial interference from both mechanical and kinematic perspectives. The results indicate that this mounting platform, relying on its mechanical yielding mechanism, can navigate misalignments and circumferential weld obstacles present in pipelines, thereby reducing the risk of the internal inspector becoming jammed during engineering operations.

5 Conclusion

Long-distance natural gas pipelines are a fundamental part of energy transportation infrastructure. Addressing engineering challenges—such as poor navigability through pipe diameter variations—faced by current in-pipe inspection equipment in large-diameter, high-pressure trunk lines, this paper uses the DN1016 trunk line of the China-Myanmar Natural Gas Pipeline as a case study. Taking into account the dimensions of bends along the route, the range of diameter variations, and pipeline topography parameters, as well as the high-pressure, high-flow operational environment, the paper employs the pipeline's actual operating pressure, medium flow velocity range, and geometric constraints as design parameters. With the aim of enhancing the pipeline robot's navigability, an internal inspection robot platform with adaptive diameter adjustment capabilities was designed. This paper focuses on the robot's structural design, theoretical modeling, multiphysics simulation, and proof-of-concept experiments. The main conclusions are as follows:

(1) Geometric constraint models for the passage through bends were established for both single-section and multi-section series-connected robots. Verification results indicate that the design parameters—an axial length of 1,450 mm for the single-section body and a center-hinged length of 183 mm for the universal joint—meet the interference-free passage requirements for a 5D bend (R = 5,080 mm) in a DN1016 pipeline, with the universal joint length falling within the theoretical safety range.

(2) Based on a quasi-static obstacle-crossing model, dual constraint conditions for traction force and anti-slip adhesion were derived. Calculations determined that the robot's maximum obstacle-crossing height is approximately 8.5 mm, providing a safety margin of 2.5 mm compared to the engineering standard requiring the circumferential weld reinforcement height within the pipe to be ≤6 mm.

(3) A multi-body dynamics simulation model for obstacle crossing was established, and parametric simulations were conducted within a speed range of 0.12–1.2 m/s, along with verification of the 8.5 mm maximum height. A rated obstacle-crossing speed of 0.24 m/s was determined: under 6 mm weld conditions, the peak torque of 12.4 N·m remained below the motor's rated value of 25 N·m, verifying the consistency between theoretical calculations and simulations.

(4) A 1:5 scaled-down proof-of-concept prototype was developed, and a simulated piping test bench was constructed. Bend passability tests verified the consistency between the three-peak oscillation characteristics and the mechanical behavior of the series-connected structure during bend traversal; obstacle-crossing tests verified the radial yielding capacity of the variable-diameter mechanism, demonstrating the feasibility of the mounted platform in reducing the risk of jamming during engineering applications.

6 Limitations and Future Work

Although this paper has achieved certain results in theoretical analysis, simulation, and experimentation, the following limitations remain: (1) The scaled-down experiments used 3D-printed PLA material, whose surface friction characteristics differ from those of the full-scale metal prototype; the accuracy of quantitative comparisons needs to be further improved. (2) The current study only analyzed the obstacle-crossing conditions for a single circumferential weld and did not address complex obstacle-crossing scenarios such as continuous obstacles or pipe-bend–weld couplings. (3) The simulation model employs an equivalent simplification of the wheel system, which fails to fully reflect the contact and collision details of the full-scale 48-wheel model.

Future work could be deepened in the following directions: Due to limitations of the experimental facility, this paper primarily validated the performance of a scaled-down proof-of-concept prototype. To advance engineering applications, subsequent research should focus on the development of a full-scale prototype. Prototype testing could be conducted using high-pressure experimental pipelines, equipped with defect detection probes, to advance the engineering application of internal inspection robots.

Data Availability

The data supporting the findings of this study are fully available within the manuscript. Reasonable requests for further clarification can be directed to the corresponding author.

References

[1] Gao Peng, Gao Zhenyu, Zhao Shangxin, et al. New progress in China's oil and gas pipeline construction in 2020 [J]. International Petroleum Economics, 2021, 29(3): 53-60.

[2] Li Qiuyang, Zhao Minghua, Ren Xuejun, et al. Construction Status and Development Trend of Chinese Oil & Gas Pipeline[J].2022(S1).

[3] Zhu Qiezhi, Wu Chao, Li Qiuyang, et al. Development status and trend of global oil and gas pipelines[J].Oil and Gas Storage and Transportation,2017,36(4):6.

[4] Liang Shuyi. Design of self-driving inspection robot with variable diameter in long-distance natural gas pipeline[D]:[Master's Thesis].Chongqing: Chongqing University of Science and Technology,2023.

[5]Xiang Jun. Design and Kinematic Analysis of a Natural Gas Driven Small-Diameter In-Pipeline Inspection Robot[D]:[Master's Thesis].Chongqing, Chongqing University,2023.

[6]Xian Lin. Design and experiment of ultrasonic internal inspection device for natural gas pipeline welds[D]:[Master's Thesis].Chengdu:Xihua University,2022.

[7]Ru Gaige. Research on Active-Passive Electromagnetic Coupling Sensing Techniques for Pipeline Inner Inspection[D]:[Doctoral Dissertation].Chengdu: University of Electronic Science and Technology of China,2023.

[8]Kim H M, Yoo H R, Park G S. A New Design of MFL Sensors for Self-Driving NDT Robot to Avoid Getting Stuck in Curved Underground Pipelines[J]. IEEE Trans. Magnetics, 2018, 54(11): 1-5.

[9]Ertugrul C, Hakan E. Design of an ex-proof untethered in-pipe inspection robot[C]. 2018: 1-6.

[10]Tourajizadeh H, et al. Dynamic Optimization of a Steerable Screw In-pipe Inspection Robot Using HJB and Turbine Installation[J]. Robotica, 2020, 38(11): 2001-2022.

[11]Zheng T, Wang X, Li H, et al. Design of a Robot for Inspecting the Multishape Pipeline Systems[J]. IEEE/ASME Trans. Mechatronics, 2022, 27(6): 4608-4618.

[12]Yu Jiuyang, Zhang De'an, Dai Yaonan, et al. Climbing Characteristic Analysis of Crawler Oil and Gas Pipeline Inspection Robot[J].Machine Tool & Hydraulics, 2023,51(15):57-61.

[13]GB/T 9711-2017 Petroleum and natural gas industries—Steel pipe for pipeline transportation systems[S].Beijing: China Standards Press,2017.

[14]Zou Shuai. Design and Kinematic Analysis of Umbrella-Shaped Pipeline Robots Based on Fluid Pressure Differentials [D].Daqing: Northeast Petroleum University,2024.

[15]Guo Penggao, Shi Lei, Hu Peiyuan, et al. Numerical Solution and Verification of Statically Indeterminate Problem of Combined Bearing for Steerable Tool[J].Bearing, 2025,(11):66-75.

[16]Zhou Qi. Design and Motion Characterization Research of Oil and Gas Pipeline Inspection Robot[D].Hefei: Anhui University of Technology,2024.

[17]Chen Shunchao. Design and dynamic Analysis of Pipe-diameter Adaptive Tracked Robot[D].Hangzhou: Hangzhou University of Electronic Science and Technology,2024.

[18]Song Yaru. Research and Development of Electro-Mechanical Integration for Variable Diameter Pipeline Robot[D].Chengdu: University of Electronic Science and Technology of China,2024.

[19]Han Yu. Design of DC Power Generation System for In-pipe Detector[D].Shenyang: Northeastern University,2020.

[20]Fang Tianyang. Structural design and dynamic analysis of a variable-diameter tracked pipeline cleaning and inspection robot[D].Hefei:Anhui Jianzhu University,2025.

[21]Zhao Pengyang. Research on motion characteristics and passability of deformable tracked pipeline robot[D].Taiyuan:North University of China,2024.

[22]Zheng Likang. Structural design and analysis of an independently driven pipeline robot with automatic pipe diameter adaptation[D].Tangshan:North China University of Science and Technology,2023.

[23]Xu Lang. Structural Design and Dynamic Research of Small-Diameter Pipeline Inspection Robot[D]. Chengdu: Southwest Petroleum University,2023.

[24]Cheng Heng. Structural Design and Motion Analysis of Small-Diameter Pipeline Inspection Robot[D]. Chengdu: Southwest Petroleum University,2023.

[25]Xie Fuzheng. Design and Research on Aerodynamically Driven Pig of Pipeline Shape Inspection[D].Qingdao: China University of Petroleum (East China),2016.

[26]Qian Jiawang. Mechanism Design and Control System Research of Mobile Robot for Narrow Pipelines[D]. Nanjing: Nanjing University of Information Science and Technology,2024.

[27]Shi Tao. Structural Design and Motion Analysis of Fluid-Driven Pipeline Robot[D]. Kunming: Kunming University of Science and Technology,2024.

[28]Huang Lianyi. Control System Design of Pipeline Robot[D]. Nanjing: Nanjing University of Science and Technology,2024.

[29]Li Jiawei. Design and Research of Pipeline Defect Inspection Robot[D]. Shanghai: Shanghai Dianji University,2024.

[30]Wang Zhao. Research on Visual Inspection and Positioning Technology of Internal Damage Detection Robot for Oil and Gas Pipelines[D]. Xi'an: Xijing University,2023.

Acknowledgments

The authors gratefully acknowledge Associate Professor Lei Shi for his valuable guidance and suggest ions throughout the research, from topic selection to paper writing. Special thanks go to Penggao Guo for h is assistance with simulation modeling and data analysis.

Author information

Authors and Affiliations
School of Mechanical Engineering, Yangtze University, Jingzhou, 434023, China
Shengqian Ruan, Lei Shi, Wangliang Xiang, Xiangjin Lin
School of Petroleum Engineering, China University of Petroleum-Beijing, 18 Fuxue Road, Changping, Beijing, P.R. China 102249
Penggao Guo

Author contributions statement

Shengqian Ruan conceived the research, conducted the theoretical analysis and simulations, performed the experiments, and wrote the original draft. Lei Shi supervised the research and reviewed the manuscript. Penggao Guo assisted with simulation modeling and data processing. Wangliang Xiang contributed to the experimental setup and data collection. Xiangjin Lin participated in the validation of simulation results and literature review. All authors reviewed and approved the final manuscript.

Corresponding author

Correspondence to Lei Shi.

Competing interests

The authors declare no known competing financial interests or personalrelationships that could influence the work reported in this paper.

Funding

This work was supported by the National Natural Science Foundation of China (Grant No. 52204002).